



Underwater nearfield blast performance of hydrothermally degraded carbon–epoxy composite structures

Helio Matos¹ · Carlos Javier¹ · James LeBlanc² · Arun Shukla¹

Received: 6 November 2017 / Accepted: 16 December 2017 / Published online: 16 January 2018
© Springer International Publishing AG, part of Springer Nature 2017

Abstract

An experimental and computational study was conducted to evaluate the dynamic response of weathered biaxial composite plates subjected to near-field explosive/blast loadings. Naval structures are subjected to aggressive marine environments during their service life that can significantly degrade their performance over time. The composite materials in this study are carbon–epoxy composite plates with [0, 90]s and [45, – 45]s layups. The composites were aged rapidly through submersion in 65 °C seawater for 35 and 70 days, which through Arrhenius' methodology, simulates approximately 10 and 20 years of operating conditions, respectively. Experiments were performed by clamping the composite plates to an air-backed enclosure inside an underwater blast facility. During the experiments, an RP-503 explosive was submerged, behind the composite specimen, and detonated. Meanwhile, transducers measured the pressure emitted by the explosive, and three high-speed cameras captured the event. Two of the cameras were placed facing the specimen to measure full field displacement, velocities, and strains through a 3D digital image correlation analysis. The third high-speed camera was used to record the explosive's behavior and bubble-to-specimen interaction. Additional experiments were performed to obtain the non-weathered and weathered material properties as well as the residual strength post the blast experiments. Additionally, a coupled Eulerian–Lagrangian finite element simulation was conducted to complement the experimental findings. Results show that the diffusion of water into the composite material leads to a more prominent blast response as well as the degradation of mechanical properties, especially shear properties which are dominated by the epoxy matrix. Residual strength experiments also show a substantial decrease in the structural integrity post-blast loading for the weathered composites. Lastly, the numerical simulations showed substantial increase in maximum strains with relatively small decreases in mechanical stiffness. Hence, even past the saturation point, incremental changes in material properties can have a significant impact on mechanical performance.

Keywords Accelerated aging · Service life · Composites · Underwater experiments · Coupled Eulerian–Lagrangian · Fluid–structure interaction

1 Introduction

An experimental and computational investigation was conducted to evaluate the dynamic response of weathered biaxial composite plates subjected to near-field explosive/blast loadings. This research arises from the concern of damage to naval and marine composite structures such as ships, submarines, and underwater vehicles (Mouritz et al. 2001; Graham-Jones

and Summerscales 2016). During the service life of these structures, their mechanical properties degrade from continuous exposure to an aggressive sea environment (Davies 2016). In undesirable circumstances, marine structures can be further subjected to shock and blast loadings. If the degradation of mechanical properties is not accounted for under these highly dynamic conditions, the damages and losses could be catastrophic.

A significant cause of mechanical degradation in composites in a marine environment is the diffusion of water into the matrix material (Davies 2016). The diffusion process is relatively well established and can be described by a diffusion coefficient that is a function of parameters such as temperature, type of resin and curing agent, surrounding medium composition, fillers, and void content. The value for diffusion

✉ Arun Shukla
shuklaa@uri.edu

¹ Dynamic Photo Mechanics Laboratory, Department of Mechanical, Industrial and Systems Engineering, The University of Rhode Island, Kingston, RI 02881, USA

² Naval Undersea Warfare Center (Division Newport), Newport, RI 02841, USA

coefficient and the theoretical models used to describe the diffusion varies in previous studies of diffusion in composites (Shirrell and Halpin 1977; Browning et al. 1977; Deiasi et al. 1980; Blikstad et al. 1984; Neumann and Marom 1987; Amer et al. 1996; Choqueuse and Davies 2008; Sar et al. 2012; Joliff et al. 2012; Fichera et al. 2015; Popineau et al. 2005; Choqueuse et al. 1997; Faguaga et al. 2012; Tual et al. 2015; Gunti et al. 2016). A standard and well-accepted model for epoxy resins, in terms of mass diffusions, is a Fickian model (Popineau et al. 2005) which uses Fick's second law to predict how the concentration of a diffusive substance changes over time within a material (Davies and Rajapakse 2014; Crank 1975).

Previous works used the Fickian model to study the properties changes during low strain rate loading of diffused composites. These studies agreed that the mechanical property degrades over time from an increase in mass, internal stresses from swelling, and loss of interlaminar strength (Choqueuse et al. 1997; Faguaga et al. 2012; Tual et al. 2015; Gunti et al. 2016). Current research on the high strain rate response of weathered composites is limited. Recently, there has been a study that analyzes the shock response of weathered composites plates within an air medium (Shillings et al. 2017). Moreover, many experimental and numerical studies analyze the dynamic response of non-weathered composite plates subjected to underwater explosives (Batra and Hassan 2007; Wei and Espinosa 2013; Leblanc and Shukla 2010, 2013; Leblanc et al. 2015).

The aim of this study is to understand how a composite's blast performance is affected by prolonged exposure to seawater. This work experimentally and computationally analyses the dynamic response of weathered composite plates subjected to nearfield underwater blasts. In the experimental portion, a 3D digital image correlation (DIC) technique is implemented to capture real-time high-speed deformation to characterize the fluid–structure interaction. In the computational portion, a coupled Eulerian–Lagrangian (CEL) simulation was used to simulate the experimental conditions to predict the composite's performance in scenarios beyond the experiments performed.

2 Experimental procedures

2.1 Composite material

2.1.1 Material manufacturing

The composite materials used consist of four unidirectional carbon fiber layers with [0, 90]s and [45, – 45]s layups. These materials were manufactured by the University of Rhode Island students at TPI Composites Inc. in Warren, RI. The composites were manufactured from two layers of $\pm 45^\circ$ biaxial carbon fabric and an epoxy resin/hardener mixture. The fabric material is Tenax HTS40 F13 24K 1600tex carbon fibers (1% polyurethane-based sizing finish) from Toho Tenax Inc. in Rockwood, TN. Also, the resin/hardener is a 100/30 weight mixture of the RIMR135/RIMH137 epoxy from Momentive Performance Materials Inc. in Waterford, NY.

The epoxy mixture was drawn into the fabric by vacuum infusion at a constant pressure of 730 mmHg. After hardening, curing was performed by placing the composite plate in an oven at 70 °C for 10 h. All specimens for both layups were cut from a single sizeable composite sheet to minimize variations in the epoxy mixture and fiber content. The final product was a 1.26 mm (0.050 in.) thick composite plate with 1% void content [(measured in accordance with ASTM Standard D2734 (2016))] and 60% fiber volume content. Table 1 lists the product information and properties of interest for the fiber, fabric, epoxy, and composite plate.

2.1.2 Mechanical testing

Quasi-static tensile and shear properties were obtained using an Instron 5585 and following ASTM Standard D3039 (2014) (with [0, 90]s specimens) and ASTM Standard D3518 (2013) (with [45, – 45]s specimens), respectively. The strain data were measured with 2-D DIC from images captured by a Prosilica camera (model GC2450 from Allied Vision Technologies GmbH in Stadroda, Germany). The tensile and shear tests were used to calculate the effective material properties used in the computational models. The strain rate sensitivity of carbon/epoxy composites, though not neg-

Table 1 Carbon and epoxy product information and properties

	Carbon fiber	Fabric	Epoxy	Composite plate
Manufacturer	Toho Tenax Inc.	Saertex LLC.	Momentive Performance Materials Inc.	University of Rhode Island
Product number	HTS40	XC611	RIMR135/RIMH137	–
Density	1600tex (linear)	602 g/m ² (areal)	1150/955 kg/m ³	1420 kg/m ³
Wet/dry glass transition temperature (°C)	–	–	72/86	72/86

ligible, is minimal (especially for normal stresses) Gilat et al. (2002); therefore, numerical results are reasonably comparable to the actual (experimental) results. Lastly, quasi-static compressive tests were performed on post-experiment specimens using ASTM Standard D7137 (2012) to measure their residual strength.

2.2 Weathering facility

The composites were submerged in a 3.5% NaCl solution [prepared in accordance with ASTM Standard D1141 (2013)] as shown in Fig. 1; this salinity matches the concentration of most ocean bodies. Before submersion, all specimens were placed in a desiccator to dry for a minimum of 72 h. In the submersion tank, four water heaters (Model LXC from PolyScience in Niles, IL) are used to maintain a constant temperature of 65 °C. It is crucial for the solution temperature to be below the wet glass transition temperature of the composite material. Beyond glass transition, there will be changes in the mechanical properties unrelated to the aging aspect of this study (Browning et al. 1977). However, a high temperature is still desired to attain a fast acceleration factor. Therefore, a temperature well under the wet glass transition was chosen to weather the experimental specimens.

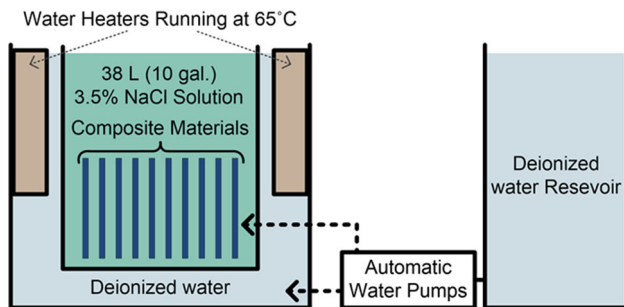
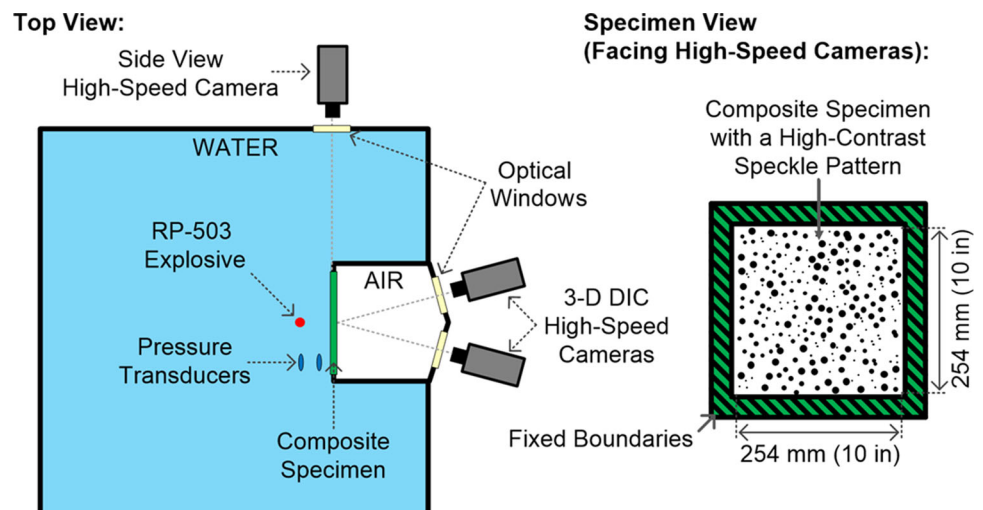


Fig. 1 Weathering facility setup

Fig. 2 Underwater blast facility and experimental setup



Float switches and water pumps are used to maintain a constant water level. As water evaporates, one float switch in the deionized water and one in the saltwater tank will independently activate water pumps to replenish the lost water. For this reason, the salinity remains constant, and water passively circulates as room temperature water is introduced. Also, the composite materials were exposed to salt water for 35 and 70 days. The blast experiments were performed immediately after the specimens left the salt water bath (to avoid moisture loss) as advised by ASTM Standard D5229 (2014).

2.3 Blast facility

2.3.1 Facility and specimen details

To perform the experiments, the underwater blast facility shown in Fig. 2 is used. This facility holds 1800 L (475 gallons) of water (where the charge is placed) and 45 L (12 gallons) of air in a chamber separated by the composite specimen. Also, the facility is made of a steel cubic shell that is dimensioned $1.2 \times 1.2 \times 1.2 \text{ m}^3$ ($4 \times 4 \times 4 \text{ ft}^3$) with a shell thickness of 12.7 mm (0.5 in.). The composite specimen is clamped between the water and air chambers with a 25.4 mm (1 in.) all-around clamping width; leaving a $254 \times 254 \text{ mm}^2$ ($10 \times 10 \text{ in.}^2$) exposed area (see Fig. 2).

An RP-503 explosive (from Teledyne RISI, San Joaquin County, CA) was used to load the composite structure. The explosive charge is composed of 454 mg RDX and 167 mg PETN contained within an outer plastic sleeve. For reference, it is energy equivalent to 1.5 g of TNT. Moreover, the charge is submerged underwater, centered to the specimen, and placed at a 152 mm (6 in.) standoff distance (additional standoff distances were also explored; see Table 2 for details). Two dynamic pressure transducers (PCB 138A05, PCB Piezotronics Inc. in Depew, NY) are located next to the

Table 2 Experimental details

Cases	Layup	Standoff distance, mm (in.)	Weathering time, days (simulated years)
E45-0wd	[45, -45]s	152 (6)	0
E45-0wd-2	[45, -45]s	114 (4.5)	0
E45-0wd-3	[45, -45]s	76 (3)	0
E45-35wd	[45, -45]s	152 (6)	35 (10)
E45-70wd	[45, -45]s	152 (6)	70 (20)
E90-0wd	[0, 90]s	152 (6)	0
E90-70wd	[0, 90]s	152 (6)	70 (20)

specimen and explosive (as illustrated in Fig. 2) at 152 mm (6 in.) and 203 mm (8 in.) distances from the explosive. During the experiments, a Dash 8HF data acquisition system (from AstroNova Inc. in Warwick, RI) captured the pressure data at two mega samples per second.

Furthermore, two Photron SA1 high-speed cameras (from Photron USA Inc. in San Diego, CA) are placed 14° apart outside the blast facility and used to record high-speed images of the specimen at 10,000 frames per second. Each image has an 832×748 spatial pixel resolution, which is approximately equivalent to 259×287 cm (10.2×11.3 in.) view from the specimen's center. The photographs from the high-speed cameras are captured through the facility's optical windows. These images are later used for the DIC analysis. Also, a third Photron SA1 camera is used (as shown in Fig. 2) to record the explosive and bubble-to-structure interactions at 10,000 frames per second (with a 576×992 spatial pixel resolution; approximately equivalent to 186×320 cm). High-intensity light sources (Super Sun-Gun SSG-400 from Frezzi Energy Systems Inc. in Hawthorne, NJ; not shown in Fig. 2) are used to illuminate the object for recording images. The details of the experimental cases are summarized in Table 2. Each experimental case has been repeated two times to validate the results (three for the E45-0WD case in Table 2).

The composite specimen's 254×254 mm² (10×10 in.²) exposed area that is facing the high-speed cameras is coated with high-contrast speckle patterns. The speckle patterns are created by randomly placing flat-white paint dots (sized 9–12 pixels per dot) on a flat-black painted background until approximately 50% of the surface area of the specimens is covered by the white dots. When clamping the composite plate, a skin layer of silicone adhesive is applied to the clamping surface to avoid water penetration into the air chamber from the clamping boundaries; therefore, during the experiments, the specimen has water and air-fluid boundaries similar to a ship hull.

2.3.2 Digital image correlation reliability

The high-speed images are analyzed using the commercially available DIC software VIC3D 7 from Correlated Solutions,

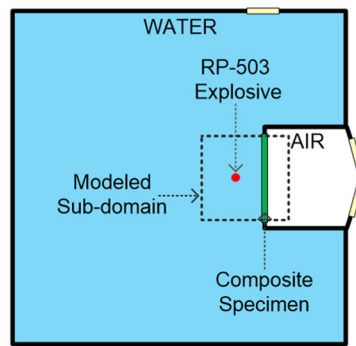
Inc., Columbia, SC. During the DIC analysis, measurements of the full-field displacements across the specimen's viewable surface are calculated by triangulating the position of each unique feature in the speckle pattern. Previous work (Gupta et al. 2014) outlines the calibration procedures that validate the accuracy of the DIC results when capturing images through an optical window (where changes in refractive index are present). It was found that the camera's viewing axis needs to be perpendicular to the optical windows in order to minimize DIC displacement errors. This technique can yield displacement errors in the order of 1.2 and 2.5% for in-plane and out-of-plane measurements, respectively.

3 Numerical model

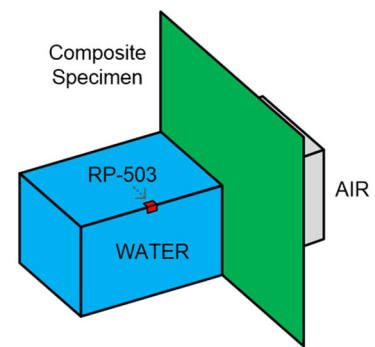
A computational finite element analysis (FEA) model similar to previous work (Leblanc et al. 2015) was created with the LS-DYNA code from the Livermore Software Technology Corp. The model uses a CEL formulation that is capable of capturing the fluid–structure interaction between the fluid and composite plate as well as an accurate representation of the explosive's detonation. All models were constructed using the CGS unit system, and simulations run in the double precision mode of LS-DYNA's Version 971, Release 9.1.0.

The FEA model consists of the air, composite specimen, water, and RP-503 charge as shown in Fig. 3. This model is representative of a subdomain from the full experimental test facility for computational efficiency. The composite specimen, 120 mm of air, and 200 mm of water is included in the modeled subdomain. The explosive is centered with respect to the composite plate with a standoff distance of 152 mm. During the experiments, the reflections from the tank walls are relatively small in magnitude and have minor effects on the composite's response. Therefore, the experiments behave as they would in a free-field condition (where no reflections are present), and the model's external fluid faces are set as non-reflecting boundaries.

All Eulerian components in the model use a combination of a material model definition and equation of state (EOS). For water, density is defined as 1 g/cm^3 , and a Gruneisen EOS

Fig. 3 Finite element model configuration**Top View:****FEA Model 3-D View**

(3 quadrants of the fluid domain is hidden):

**Table 3** RDX and JWL EOS material parameters (Dobratz 1972)

ρ (explosive density)	1.77 g/cm ³
D (detonation velocity)	850e3 cm/s
E_o (detonation energy per unit volume)	5.93e10 dyn/cm ²
P (Chapman–Jouguet pressure)	3.41e13 dyn/cm ²
A (JWL linear coefficient)	7.78e12 dyn/cm ²
B (JWL linear coefficient)	7.07e11 dyn/cm ²
$R1$ (JWL nonlinear coefficient)	4.485
$R2$ (JWL nonlinear coefficient)	1.068
ω (JWL nonlinear coefficient)	0.3

Table 4 Numerical cases details

Cases	Layup	Weathering exposure (days)
C45-0wd	[45, -45]s	0
C45-35wd	[45, -45]s	35
C45-70wd	[45, -45]s	70
C90-0wd	[0, 90]s	0
C90-35wd	[0, 90]s	35
C90-70wd	[0, 90]s	70

is used with a sound speed of 149,000 cm/s. For air, density is defined as 0.0013 g/cm³ and a Linear Polynomial EOS is used as a gamma law EOS (where $C_0 = C_1 = C_2 = C_3 = C_6 = 0$ and $C_4 = C_5 = \gamma - 1 = 0.4$). The RP-503 explosive is created with a JWL EOS by assuming that it is composed of 621 mg of RDX instead of the actual 454 mg of RDX and 167 mg of PETN. This assumption is acceptable since the explosive is mostly RDX and the JWL coefficient of the PETN is similar to the RDX's. The explosive's physical and JWL EOS parameters are provided in Table 3. More details about EOS models and assumptions can be found in previous work (Leblanc et al. 2015).

The composite plate is modeled using 3D continuum solid elements through the thickness of the plate. Solid elements were used instead of shell elements to estimate interlaminar stresses/strains. Each ply of the composite laminate is represented by a single layer of solids, with 4 in total through the thickness. For the boundary conditions, the plate's out-of-plane displacements and rotations were fully constrained at its edges. Also, during the experiments, slippage on the clamped edges in the order of 1 mm was observed. Hence, no in-plane restrictions were applied. The amount of edge slippage from the numerical simulations is consistent with DIC measurements. This slippage was caused by the overwhelming loading magnitudes which over-

came the clamping friction. Moreover, the density of the plate was set to 1.42 g/cm³, and the effective stiffness of the plate is defined in Sect. 4.2. Lastly, the composite damage was modeled by LS-Dyna's Mat_Composite_Damage (Mat_022). This material definition encompasses failure criteria of tensile, compression, and in-plane shear.

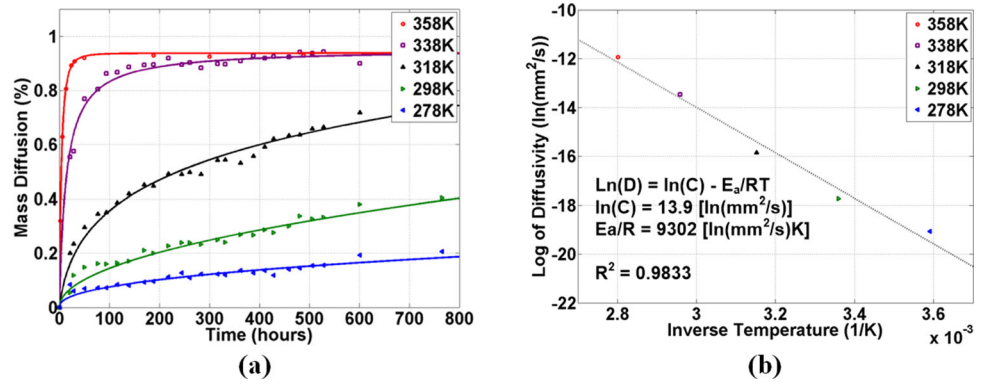
The loading on the composite plates occurs in a two-step process. First, a quasi-static pressure (from the water column weight) is uniformly applied over the face of the plate. Subsequently, the explosive detonation is initiated which leads to a transient response of the composite plate. In the computational part of this study, six different numerical cases are analyzed as shown in Table 4. The cases consist of the 2 layup configurations, [0, 90]s and [45/-45]s with three levels of weathering (0, 35, and 70 days). All cases are evaluated with the 152 mm charge standoff scenario.

4 Results and discussion

4.1 Weathering

From Arrhenius' methodology, the water diffusion activation energy (E_a) for an epoxy is assumed to be constant (Rice 2011). Therefore, a mass diffusion study was performed at various temperatures (different diffusion rates) to obtain a diffusion acceleration factor (AF) with respect to a specific

Fig. 4 **a** Mass diffusion for five temperatures and **b** logarithmic relationship between diffusivity and temperature



temperature. The moisture absorption was measured for composites submerged in 3.5% NaCl solutions at 5, 25, 45, 65, and 85 °C in accordance with ASTM Standard D5229 (2014). Note that the wet glass transition temperature (72 °C) is based on the composite’s storage modulus and not its diffusion activation energy. The composite’s diffusivity still follows Arrhenius’ methodology at 85 °C even though its stiffness is lower at this temperature. Therefore, this high temperature is only used for the mass diffusion study and not for weathering the experimental specimen.

The water diffusivity into the composite plate obeys Fick’s second law of diffusion (Davies and Rajapakse 2014). Fick’s second law was simplified into one dimension to calculate the diffusion coefficient (D) using Eq. (1) (Crank 1975). The diffusion coefficient was calculated from a point that is within the initial linear portion of the mass diffusion curve ($\leq 50\%$ mass saturation). The diffusion coefficient was related to E_a using Arrhenius’ equation. To solve for E_a , Eq. (2) was written in logarithmic form as shown in Eq. (3), then $-E_a/R$ was found as the slope of the linear trend for the various diffusion temperatures (Crank 1975). Figure 4a, b shows the mass diffusion for different temperatures and the logarithmic relationship between D and E_a respectively; the markers in Fig. 4 represents measured experimental data while the line trends are the estimated exponential functions used to extrapolate values needed.

$$D = \frac{\pi}{t} \left(\frac{h M_t}{4 M_s} \right)^2, \tag{1}$$

$$D = C e^{-\frac{E_a}{RT}}, \tag{2}$$

$$\ln(D) = \ln(C) - \frac{E_a}{RT}, \tag{3}$$

where t is time; M_t is the composite’s mass at time t ; M_s is the composite’s saturated mass; h is the composite plate’s thickness; C is the diffusion constant; R is the universal gas constant; and T is the temperature in the absolute scale.

After obtaining the activation energy for the composite material, AF can be found as the ratio of diffusions at different temperatures as shown in Eq. (4) (Rice 2011). The submersion specimens were kept at a constant temperature ($T_1 = 338$ K), but the service temperature (T_2) can vary depending on the application. Hence, AF is application dependent. For reference, if the average ocean temperature (17 °C) is assumed to be the operational temperature, then 35 and 70 days of submersion approximates to 10 and 20 years of service, respectively.

$$AF = \frac{C e^{-\frac{E_a}{RT_2}}}{C e^{-\frac{E_a}{RT_1}}} = e^{\left(\frac{E_a}{R}\right)\left(\frac{T_2 - T_1}{T_1 T_2}\right)} \tag{4}$$

4.2 Mechanical properties

In the material model, a plane stress assumption is used for the composite plate. The materials tested were from the same batch of materials used to for the experimental specimen. Therefore, effective properties (homogenized laminate properties) Vaughan and Gilbert (2001) were measured instead of

Table 5 Composite’s effective mechanical properties

Weathering time (days)	0	35	70
E_x, E_y (GPa)	78.4 ± 1.8	78.0 ± 2.1	74.9 ± 2.6
V_{xy}	0.039 ± 0.014	0.040 ± 0.010	0.042 ± 0.009
Failure normal strain (%)	1.46 ± 0.09	1.38 ± 0.09	1.36 ± 0.07
G_{xy} (GPa)	7.38 ± 0.19	5.32 ± 0.24	4.92 ± 0.22
Yield shear stress (kPa)	36.1 ± 1.1	25.3 ± 1.0	21.7 ± 0.6
Failure shear stress (kPa)	45.3 ± 1.2	41.3 ± 1.9	38.7 ± 2.6
Failure shear strain (%)	4.92 ± 0.79	7.25 ± 0.25	7.28 ± 0.89

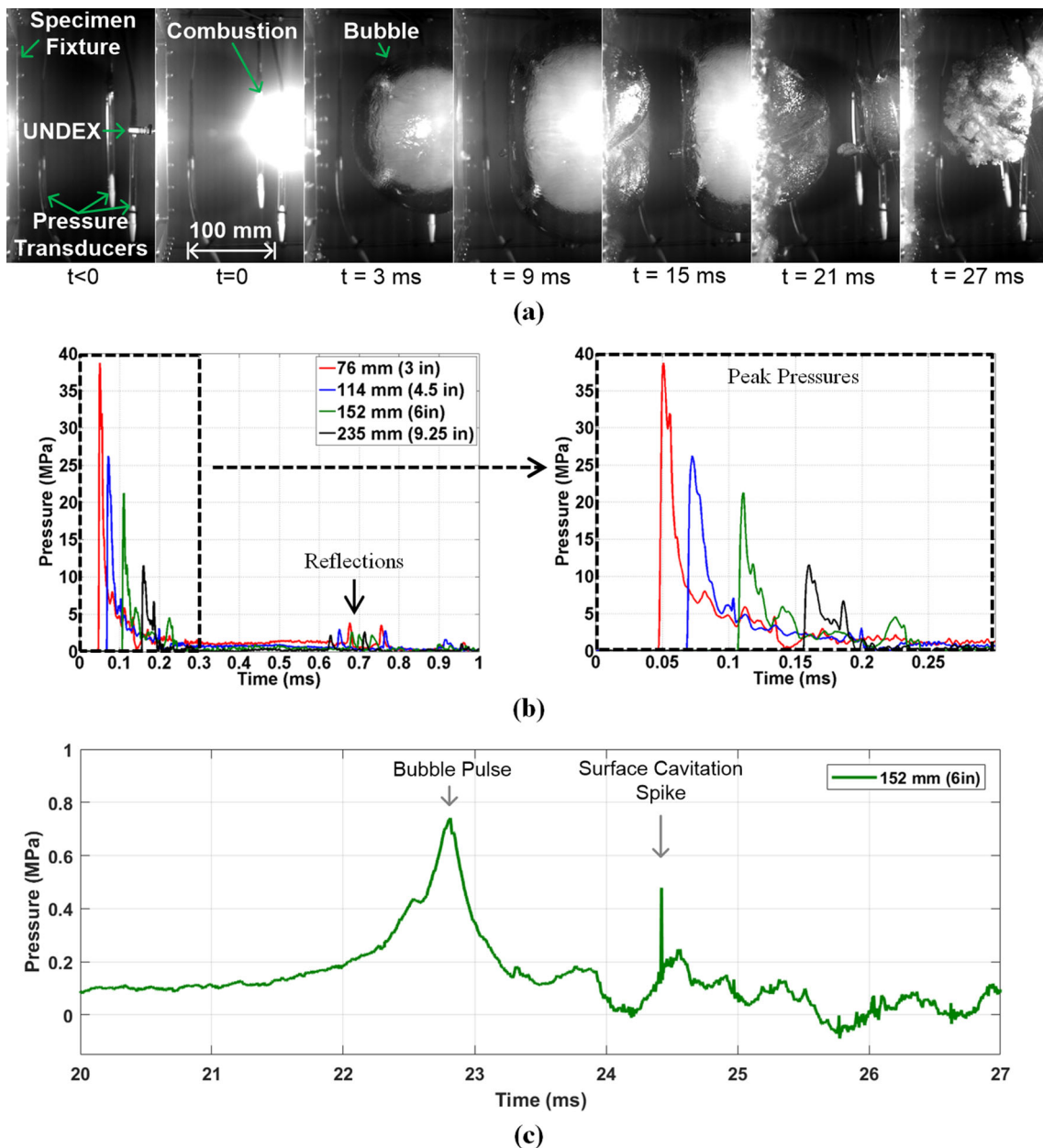


Fig. 5 a Fluid–structure interaction images, b pressure history from the explosive, and c bubble as well as surface cavitation pressure pulses

ply properties. Table 5 shows the effective elastic modulus (E_x and E_y), Poisson’s ratio (ν_{xy}), shear modulus (G_{xy}), and failure strains which were calculated with the standards outlined in Sect. 2. The effective elastic modulus was the same in both principal directions ($E_x = E_y$) since the layup is symmetric and evenly balanced. The normal stress has a linear behavior until failure, but the shear stress has a bilinear behavior; the shear yield and failure stresses are also listed in Table 5. Each result for the effective material properties in Table 5 is calculated from six tests.

4.3 Blast response

During the experiments, the RP-503 underwater explosive (UNDEX) combusts at $t = 0$ as shown in Fig. 5a. The high pressures from the explosive loads the composite specimen and also leads to the formation of a cavitation bubble at the charge location at $t = 3$ ms. The cavitation bubble expands spherically until it begins to interact with the composite plate. As a result, its growth is skewed away from the composite.

The bubble's expansion peaks at $t = 9$ ms, which is when the bubble begins to collapse from its low internal cavitation pressure and high external pressure. During this collapse, the surrounding fluid accelerates towards the bubble, which leads to a new surface cavitation on the composite due to its close proximity as seen in Fig. 5a at $t = 15$ ms. When the bubble finally collapses at $t = 22$ ms, the composite's surface is fully engulfed by this new surface cavitation. Therefore, the composite specimen does not react to the bubble collapse. However, the pressures from the bubble collapse initiate the surface cavitation collapse, which does so at $t = 24$ ms. The bubble pulsation cycle is interrupted by the surface cavitation collapse; hence the loading cycles of interest are completed by this time.

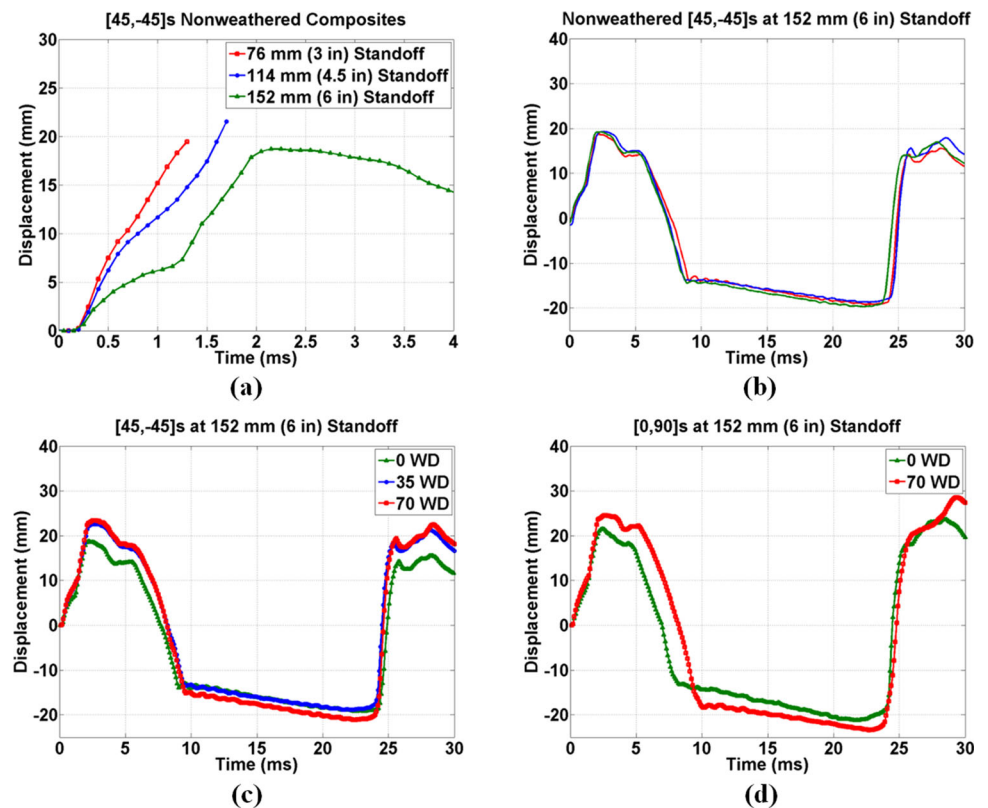
Moreover, the high pressures from the explosive are shown in Fig. 5b for different distances (each measured during a different experiment). The shock from the explosive is distinguished by an immediate rise in pressure followed by exponential decay. The amplitude of the explosive pressure decreases spherically by $1/R$ from the explosive location. When the explosive pressures are normalized in time for charge distance and in magnitude by $1/R$, the pressure trends are nearly identical; hence the loading condition is highly repeatable between experiments. Also, the reflections from the tank's boundaries are small relative to the initial explosive pressures. Furthermore, the pressure from the bubble pulse and surface cavitation collapse are shown in Fig. 5c for the

152 mm standoff case. The bubble pulse has a comparable impulse to the initial explosive pulse due to its long duration. The surface cavitation collapse has low recorded pressure signatures. However, pressure signatures at this point in time are partially blocked by the bubble. Even so, an acoustic spike is seen when the surface cavitation's water boundary slaps against the composite plate, which leads to a substantial amount of momentum transfer to the composite. Additionally, the bubble pulse was nearly identical in magnitude as well as duration between experiments and the surface cavitation spike is only consistent in time (not shown in Fig. 5c).

4.4 Deformation and image analysis

The out of plane deformation from the 3D DIC is illustrated in Fig. 6, which shows center point displacements. Each of the displacement curve shown is from one representative experiment. The center point displacements for the non-weathered [45, -45]s composite plate at different standoff distances is shown in Fig. 6a. Decreasing the standoff distance leads to higher loading pressure and higher deformation rates. The displacement curves for the 76 and 114 mm standoff ended when failure (in the form of through-thickness cracking) is observed during the experiment (in the high-speed images). For the 152 mm standoff distance, failure is not observed during the experiments but is seen during the post-mortem analysis.

Fig. 6 Center point displacements for **a** [45, -45]s non-weathered composites at different standoff distances, **b** [45, -45]s non-weathered composite at 152 mm (6 in.) standoff, **c** [45, -45]s weathered composites, and **d** [0, 90]s weathered composites



As loading initiated on the composite’s surface, it flexes towards the air-side (forward) to a maximum displacement. When the composite begins to rebound, the surface cavitation (at vacuum pressure) begins at 8 ms, and the specimen rapidly abruptly flexes towards its water side (backward) to a magnitude beyond its initial displacement (seen 8 and 24 ms). At $t = 24$ ms, the surface cavitation collapses, and an abrupt increase in displacement forward occurs once again as shown by the full displacement cycle in Fig. 6b. Figure 6b also illustrates the repeatability of the three experiments for the E45-0wd case.

Weathering the composite plates led to an increase in maximum displacements for the same loading condition. The center point displacement curves for the [45, –45]s composite plates at 152 mm (6 in) standoff are shown in Fig. 6c for the non-weathered, 35 weathering days (WD), and 70 WD cases. After weathering the [45, –45]s composite for 35 days, the maximum center point displacements increase by an average of 20%. An additional 5% increase in displacement is seen for the 70 WD cases, which is a further decrease in performance post-saturation. The response in 70 WD from 35 WD could be halted by the increase in damage as it will be shown in the next section. Also, the stiffness of a fully clamped plate increases with deformation; hence, further changes from a highly deformed plate are countered by immense resistance. The [0, 90]s composite plates behaved similarly to the [45, –45]s plates. The 70 WD case for the [0, 90]s layup had a center point displacement 15% higher than the non-weathered case as shown in Fig. 6d.

4.5 Composite post-mortem

The post-mortem analysis revealed that damage increased with weathering time. The main type of damage for the [45, –45]s cases was interfibrillar, and through-thickness damage near the plate’s corners is illustrated in Fig. 7a. In terms of the 35 WD and 70 WD, there is a notable increase in average crack length. This increase in crack length suggests further material degradation from fiber/matrix debonding after saturation. For the [0, 90]s cases, the damage was predominately seen in the form of delamination near its corners (not shown in Fig. 7). Weathering the [0, 90]s specimen showed an increase in damage in terms of increased delamination area. The difference in damage between [45, –45]s and [0, 90]s arises from how the boundary interacts with the fiber orientation. The deformation mode for a plate (mode 1) has diagonal lobes. Hence, high strain levels diagonally and matrix cracking (through-thickness) in the [45, –45]s plates. Also, when the fiber direction is not perfectly aligned with the deformation lobes, interfibrillar cracking occurs during the through thickness crack propagation. For the [0, 90]s, the diagonal lobes lead to bend and twisting of the fibers, which forces debonding/delamination. Fig. 7b shows the relative increase in average crack length for the [45, –45]s cases, and the relative increase in delamination area for the [0, 90]s cases. Based on the [45, –45]s crack lengths, the damage levels seem to increase with weathering time consistently.

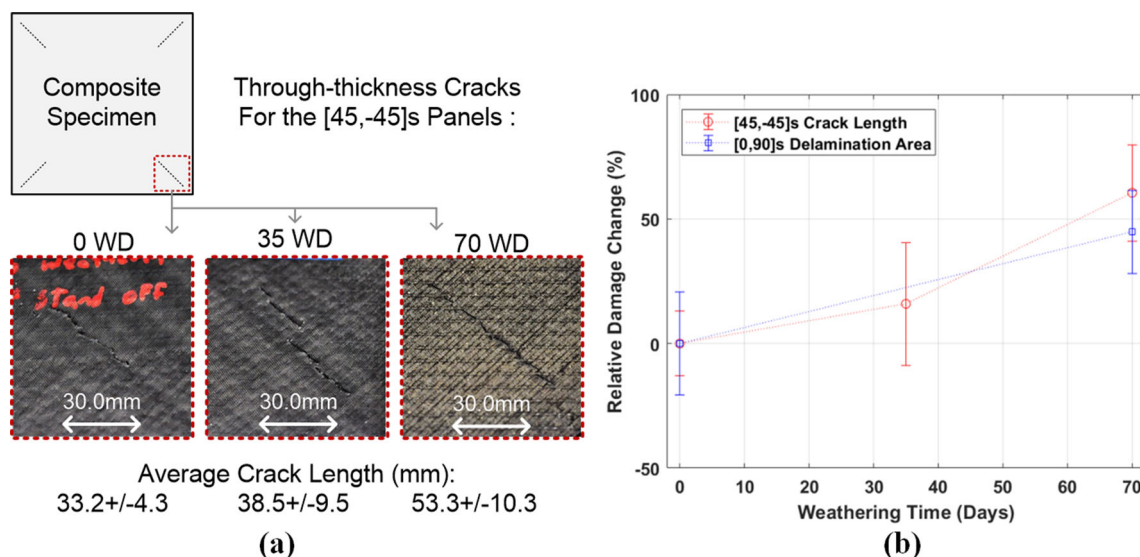


Fig. 7 a Interfibrillar and through-thickness cracking for the [45, –45]s cases and b relative change in damage

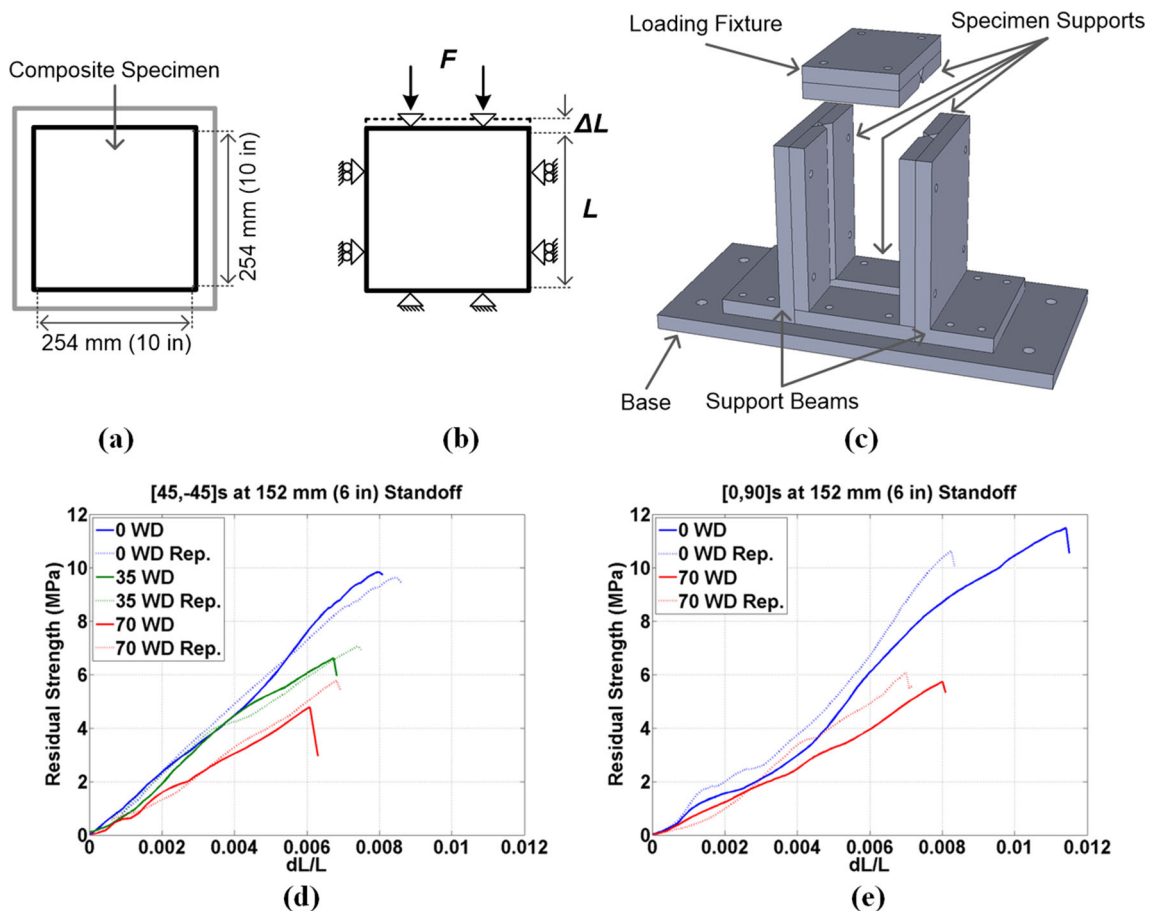


Fig. 8 Residual strength for the **a** $[45, -45]_s$ weathered composites, and **b** $[0, 90]_s$ weathered composites

4.6 Residual strength

Quasi-static compressive tests were performed on specimens after the explosive/blast experiments using ASTM Standard D7137 (2012) to measure and compare compressive residual strength properties between non-weathered and weathered samples. To perform this residual strength tests, the composite specimen was simply supported at the $254 \times 254 \text{ mm}^2$ ($10 \times 10 \text{ in.}^2$) central area (same boundary locations as the blast experiments) as shown in Fig. 8a. A schematic of the boundary and loading condition is shown in Fig. 8b as well as a model for the loading fixture in Fig. 8c. Figures 8d, e shows the load applied in units of MPa versus the relative change in length for the $[45, -45]_s$ and $[0, 90]_s$ cases, respectively. For the $[45, -45]_s$ cases, the average ultimate strength decreases by 29.6% after 35 WD, and 45.7% after 70 WD. For the $[0, 90]_s$ cases, the average residual strength decreases by 46.5% after 70 WD.

During blast experiments, the difference in performance between the 35 WD and 70 WD cases is not very distinguishable. However, a substantial decrease in residual strength is observed between the 35 WD and 70 WD cases. This is

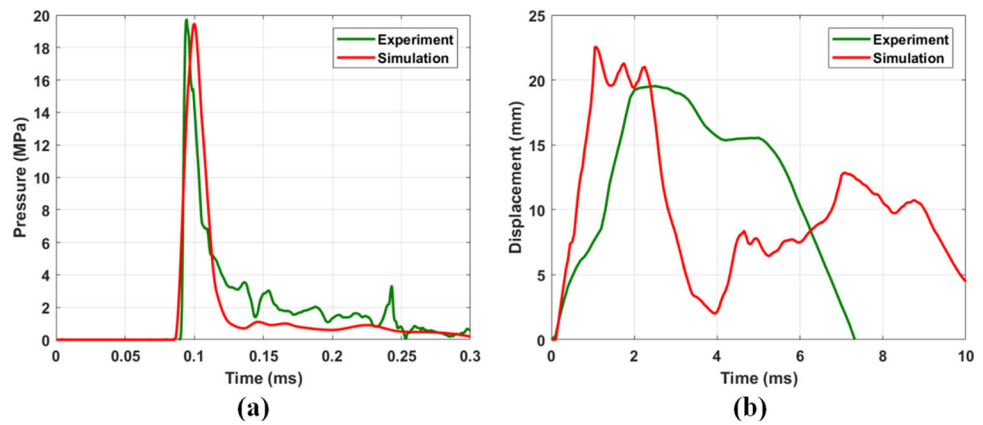
consistent with what was observed during the post-mortem. For this reason, it is shown that material degradation for carbon/epoxy composites occurs even after saturation from additional chemical processes.

5 Numerical results

5.1 Numerical model correlation

The correlation between the computational model and the corresponding experiment in terms of the UNDEX pressure profile is shown in Fig. 9a as measured by the 152 mm stand-off. The experimental trends seen in Fig. 9a, b were selected from a representative experiment; experimental variation is shown in Fig. 6b. In Fig. 9a, the peak pressure predicted by the simulation is nearly identical to the value observed during the experiment. The simulation shows a longer rise time and similar decay time. The overall impulse between the two signals is comparable; hence, the UNDEX EOS definition and parameters are deemed to be appropriate for this model. Furthermore, the tank reflections were relatively small compared

Fig. 9 Numerical and experimental comparison in terms of **a** pressure history at 152 mm from the explosive, and **b** center point displacements for the [45, −45]s non-weathered case



to the initial load. Therefore, the non-reflective boundary condition is also appropriate for this model.

The transient displacement time history of the center point displacement for the E45-0wd and C45-0wd cases is shown in Fig. 9b. The model captured the peak center point displacements relatively well, with the simulations overpredicting the peak by ~10–15%. However, the simulations show notable discrepancies during the flexural motion of the composite. The first discrepancy is the prolonged response in deformation seen between 0.5 and 1.25 ms in the experiments. This same prolonged response behavior in the experimental data can be seen after the plate reaches its maximum displacement and starts to recoil between 3.5 and 5 ms. These discrepancies are believed to be the result of an underdefined material model. The numerical model was from the effective stiffness (homogenized laminate properties) of the composite. Hence, the full stiffness matrix or any rate dependency was not specified in the model. With the current material model, things such as delamination and other out-of-plane failure mechanisms cannot be accounted for. However, the maximum displacements and, in turn, maximum strains, can still be predicted by the current material model. Moreover, the displacement velocities leading up to the maximum displacement, and velocities that soon follow, are well matched during the simulations. Lastly, the surface cavitation to composite interaction was not predicted by the numerical model. Therefore, nothing after the maximum displacements/strains will be considered in the following discussions.

5.2 Maximum strains

The maximum in-plane ϵ_{xx} strain field for the [45, −45]s non-weathered numerical model is shown in Fig. 10a. For all simulations, ϵ_{xx} and ϵ_{yy} are nearly the same; hence, they will just be referred to as normal strains. The maximum normal strains are located in the lobes of the buckling mode, at 57.2 mm (2.25 in.) away from the corners. Moreover, the maximum strains (normal and shear) for all numerical cases

are listed in Table 6. The values in Table 6 are greater than the failure strains listed in Table 5. These higher values are expected since the transverse composite properties are not incorporated into the failure model. However, the maximum simulation strains are still valuable information because they illustrate how the weathering affects strain levels.

The maximum strain values from Table 6 are used to calculate the relative failure probability as a function of weathering time with Eq. (5), where the maximum strains (normal and shear) are subtracted from the non-weathered case strains then divided by its respective failure strain (listed in Table 5). The results from this calculation are illustrated in Fig. 10b. Based on the normal strain data, failures from normal stresses are strongly proportional to weathering time regardless of saturation level. From the shear strain data, it is unclear if there is a relationship between failure from shear stresses and weathering time. All maximum strain values increase with weathering time. However, the epoxy matrix itself becomes more compliant (as shown by the decrease in stiffness and higher failure strains in Table 5), which offsets the failure probability as defined by Eq. (5). Furthermore, there is also a proportional relationship between the failure probability from normal stresses and damage accumulation in terms of through-thickness cracking for the [45, −45]s cases as illustrated in Fig. 10c. In turn, damage accumulation is also proportional to weathering time regardless of saturation levels as it was inferred by Fig. 7b.

$$\left(\frac{\epsilon_{\max} - \epsilon_{\max | \text{WD}=0}}{\epsilon_{\text{failure}}} \right) 100 \tag{5}$$

5.3 Stress evolution

A comparison of the stress field in the [45, −45] and [0, 90]s laminates is shown in Fig. 11 for the no weathering cases. The evolution and propagation of the stress field out to the plate boundaries through time illustrate several trends regarding the plate load distribution. Foremost the areas of highest stresses are located in different areas of the plates

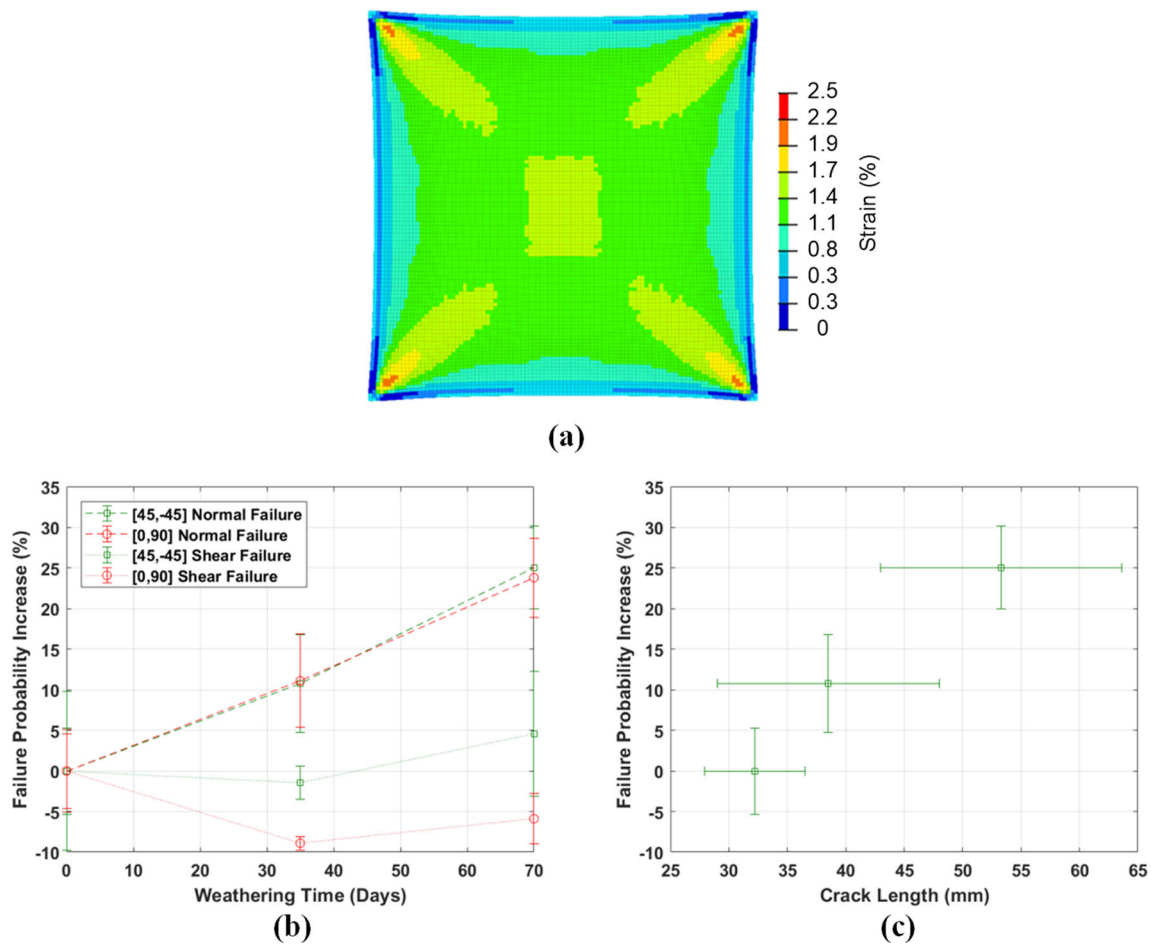


Fig. 10 **a** ϵ_{xx} strain distribution for the numerical model at $t = 1.1$ ms, **b** relative change in failure probability vs weathering time, and **c** relative change in failure probability vs through-thickness crack length for the [45, -45]s cases

for the respective configurations and also occur at different points in time during the loading. The [45, -45]s case sustains the highest stress state in the way of the corners with the peak stress occurring at ~ 0.2 ms after the onset of pressure loading. Conversely, the [0, 90]s case sustains the highest magnitude of stress along the vertical and horizontal plate edges and is highly localized along a thin line. The highest stresses in the [0, 90]s laminates occur at 0.40 ms, later in time than the peak stresses in the [45, -45] cases. This illustrates how the laminate orientation could be used as “stress guides” to direct the high stresses to areas in a structure (or boundary) that are stronger or have higher dissipation properties (in the case of hybrid composites).

6 Conclusions

This work experimentally and numerically analyzed the dynamic response of weathered composite plates subjected to nearfield underwater blasts from explosives. The aim of

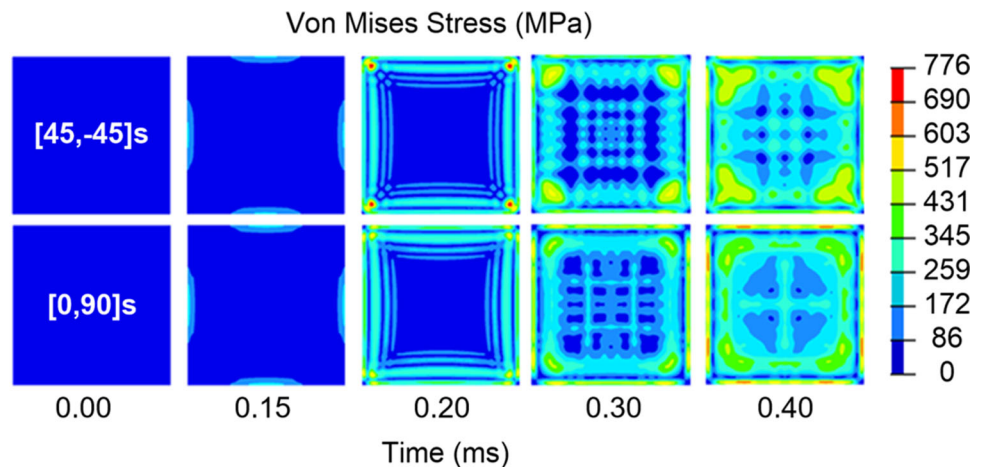
Table 6 Maximum strains for composite simulations with a 152 mm (6 in.) standoff

Cases	Maximum strains, ϵ_{\max} (%)	
	$\epsilon_{xx} / \epsilon_{yy}$	ϵ_{xy}
C45-0wd	2.51	5.83
C45-35wd	2.52	8.63
C45-70wd	2.68	9.02
C90-0wd	2.41	2.74
C90-35wd	2.43	3.46
C90-70wd	2.57	3.66

this study was to understand better how a composite plate’s blast performance is affected by prolonged exposure to seawater. The main findings of this study are as follows:

- The mechanical properties of the carbon–epoxy composites degraded even after its saturation point (after 35 days of weathering) during hydrothermal degradation. Most

Fig. 11 Stress field evolution after charge combustion



- notably, the shear properties had the highest degradation, which is governed by the matrix material.
- The maximum center point displacements during the blast experiments for the [45, −45]s composite increased (+20%) between the non-weathered and 35 WD specimen. Only a small increase in displacements (+5%) was attained by doubling the exposure to 70 WD. Similarly, for the [0, 90]s composites, a 70 WD exposure yielded a 15% higher than the non-weathered case.
 - The damage accumulation increased with weathering time during the post-mortem analysis. The predominant damage type is also different for the two layup configurations. For the [45, −45]s cases, interfibrillar and through-thickness cracking was the primary type of damage. For the [0, 90]s cases, delamination was the main type of damage. Also, the damage locations are consistent with lobe locations for a mode 1 plate deformation as it would be expected.
 - Residual strength experiments showed a significant decrease in performance between the 35 WD and 70 WD cases in comparison to the blast experiments. This decrease in performance is consistent with the increase in damage levels measured during the post-mortem. This illustrates how material degradation occurs after saturation. For the [45, −45]s composite plates, the average residual strength decreased by 30% for the 35 WD case, and 46% for the 70 WD when compared to the non-weathered case.
 - The effective material properties used in the numerical model led to discrepancies such as simulation rise time and rebound behavior. However, the properties and EOS used in the model was able to predict center point peak displacements, deformation shape, and explosive loading profile. In the future, properties should be obtained from parallel laminates at different angles as well as strain rates and use CLT to build rate-dependent stiffness matrices; this would likely require a user subroutine to define the

material in numerical codes. Also, high rate failure properties should be obtained for future studies.

- Based on the normal strain data from Tables 5 and 6, failures from normal stresses are strongly proportional to weathering time regardless of saturation level. From the shear strain data, it is unclear if there is a relationship between failures from shear stresses and weathering time.
- Failure probability from normal stresses is proportional to damage accumulation in terms of through-thickness cracking for the [45, −45]s cases as illustrated in Fig. 10c. In turn, damage accumulation is also proportional to weathering time regardless of saturation levels as it was inferred by Fig. 7b and previous conclusion.
- The laminate orientation could be used as “stress guides” to direct the high stresses to areas in a structure (or boundary) that are stronger or has higher dissipation properties for dynamic applications.

Acknowledgements The authors kindly acknowledge the financial support provided by Mr. Kirk Jenne and Dr. Elizabeth Magliula from the Naval Engineering Education Consortium (NEEC) under Grant no. N00174-16-C-0012; the composite expertise and manufacturing support from Tim Fallon and Mike Trapela from TPI Composites in Warren, RI; and the assistance in designing the residual strength fixture by Professor Valentina Lopresto from the University of Naples Federico II [Università degli Studi di Napoli Federico II] in Naples, Italy.

Compliance with ethical standards

Conflict of interest On behalf of all authors, the corresponding author states that there is no conflict of interest with the contents of this manuscript.

References

- Amer M, Koczak M, Schadler L (1996) Relating hydrothermal degradation in single fiber composites to degradation behavior in bulk

- composites. *Compos A Appl Sci Manuf* 27(9):861–867. [https://doi.org/10.1016/1359-835x\(96\)00049-8](https://doi.org/10.1016/1359-835x(96)00049-8)
- ASTM Standard D1141-98 (2013) Standard practice for the preparation of substitute ocean water. ASTM International, West Conshohocken. <https://doi.org/10.1520/D1141-98R13>
- ASTM Standard D2734-16 (2016) Standard test methods for void content of reinforced plastics. ASTM International, West Conshohocken. <https://doi.org/10.1520/D2734-16>
- ASTM Standard D3039-14 (2014) Standard test method for tensile properties of polymer matrix composite materials. ASTM International, West Conshohocken. https://doi.org/10.1520/D3039_D3039M-14
- ASTM Standard D3518-13 (2013) Standard test method for in-plane shear response of polymer matrix composite materials by tensile test of a $\pm 45^\circ$ laminate. ASTM International, West Conshohocken. https://doi.org/10.1520/D3518_D3518M
- ASTM Standard D5229-14 (2014) Standard test method for moisture absorption properties and equilibrium conditioning of polymer matrix composite materials. ASTM International, West Conshohocken. https://doi.org/10.1520/D5229_D5229M-14
- ASTM Standard D7137-12 (2012) Standard test method for compressive residual strength properties of damaged polymer matrix composite plates. ASTM International, West Conshohocken. https://doi.org/10.1520/D7137_D7137M-12
- Batra R, Hassan N (2007) Response of fiber reinforced composites to underwater explosive loads. *Compos B Eng* 38(4):448–468. <https://doi.org/10.1016/j.compositesb.2006.09.001>
- Blikstad M, Sjoblom PO, Johannesson TR (1984) Long-term moisture absorption in graphite/epoxy angle-ply laminates. *J Compos Mater* 18(1):32–46. <https://doi.org/10.1177/002199838401800103>
- Browning C, Husman G, Whitney J (1977) Moisture effects in epoxy matrix composites. In: Davis J (ed) *Composite materials: testing and design* (fourth conference), STP26961S. ASTM International, West Conshohocken, PA, pp 481–496. <https://doi.org/10.1520/STP26961S>
- Choqueuse D, Davies P (2008) Aging of composites in underwater applications. *Aging Compos*. <https://doi.org/10.1201/9781439832493.ch18>
- Choqueuse D, Davies P, Mazéas F, Baizeau R (1997) Aging of composites in water: comparison of five materials in terms of absorption kinetics and evolution of mechanical properties. In: *High temperature and environmental effects on polymeric composites*, vol 2. <https://doi.org/10.1520/stp11369s>
- Crank J (1975) *The mathematics of diffusion*, 2nd edn. Oxford University Press, Oxford
- Davies P (2016) Environmental degradation of composites for marine structures: new materials and new applications. *Philos Trans R Soc A Math Phys Eng Sci* 374(2071):20150272. <https://doi.org/10.1098/rsta.2015.0272>
- Davies P, Rajapakse Y (2014) Durability of composites in a marine environment. Springer, Dordrecht
- Deiasi RJ, Whiteside JB, Wolter W (1980) Effects of varying hygrothermal environments on moisture absorption in epoxy composites. In: *Fibrous composites in structural design*. pp 809–818. https://doi.org/10.1007/978-1-4684-1033-4_48
- Dobratz B (1972) Properties of chemical explosives and explosive simulants. Lawrence Livermore National Laboratory, Livermore. <https://doi.org/10.2172/4285272>
- Faguaga E, Pérez C, Villarreal N, Rodriguez E, Alvarez V (2012) Effect of water absorption on the dynamic mechanical properties of composites used for windmill blades. *Mater Des* (1980–2015) 36:609–616. <https://doi.org/10.1016/j.matdes.2011.11.059>
- Fichera M, Totten K, Carlsson LA (2015) Seawater effects on transverse tensile strength of carbon/vinyl ester as determined from single-fiber and macroscopic specimens. *J Mater Sci* 50(22):7248–7261. <https://doi.org/10.1007/s10853-015-9279-3>
- Gilat A, Goldberg RK, Roberts GD (2002) Experimental study of strain-rate-dependent behavior of carbon/epoxy composite. *Compos Sci Technol* 62(10–11):1469–1476. [https://doi.org/10.1016/S0266-3538\(02\)00100-8](https://doi.org/10.1016/S0266-3538(02)00100-8)
- Graham-Jones J, Summerscales J (2016) *Marine applications of advanced fibre-reinforced composites*. Woodhead Publishing, Sawston. <https://doi.org/10.1016/c2013-0-16504-x>
- Gunti R, Prasad AR, Gupta A (2016) Mechanical and degradation properties of natural fiber reinforced PLA composites: jute, sisal, and elephant grass. *Polym Compos*. <https://doi.org/10.1002/pc.24041>
- Gupta S, Parameswaran V, Sutton MA, Shukla A (2014) Study of dynamic underwater implosion mechanics using digital image correlation. *Proc R Soc A Math Phys Eng Sci* 470(2172):20140576–20140576. <https://doi.org/10.1098/rspa.2014.0576>
- Joliff Y, Belec L, Heman M, Chailan J (2012) Experimental, analytical and numerical study of water diffusion in unidirectional composite materials—interphase impact. *Comput Mater Sci* 64:141–145. <https://doi.org/10.1016/j.commatsci.2012.05.029>
- Leblanc J, Shukla A (2010) Dynamic response and damage evolution in composite materials subjected to underwater explosive loading: an experimental and computational study. *Compos Struct* 92(10):2421–2430. <https://doi.org/10.1016/j.compstruct.2010.02.017>
- Leblanc J, Shillings C, Gauch E, Livolsi F, Shukla A (2015) Near field underwater explosion response of polyurea coated composite plates. *Exp Mech* 56(4):569–581. <https://doi.org/10.1007/s11340-015-0071-8>
- Leblanc J, Shukla A (2013) Underwater explosive response of submerged, air-backed composite materials: experimental and computational studies. *Blast Mitig* 123–160. https://doi.org/10.1007/978-1-4614-7267-4_5
- Mouritz A, Gellert E, Burchill P, Challis K (2001) Review of advanced composite structures for naval ships and submarines. *Compos Struct* 53(1):21–42. [https://doi.org/10.1016/S0263-8223\(00\)00175-6](https://doi.org/10.1016/S0263-8223(00)00175-6)
- Neumann S, Marom G (1987) Prediction of moisture diffusion parameters in composite materials under stress. *J Compos Mater* 21(1):68–80. <https://doi.org/10.1177/002199838702100105>
- Popineau S, Rondeau-Mouro C, Sulpice-Gaillet C, Shanahan ME (2005) Free/bound water absorption in an epoxy adhesive. *Polymer* 46(24):10733–10740. <https://doi.org/10.1016/j.polymer.2005.09.008>
- Rice M (2011) Activation energy calculation for the diffusion of water into PR-1590 and pellethane 2103-80AW polyurethanes. NUWC-NPT Technical Memo 11-062
- Sar B, Fréour S, Davies P, Jacquemin F (2012) Coupling moisture diffusion and internal mechanical states in polymers—a thermodynamical approach. *Eur J Mech A Solids* 36:38–43. <https://doi.org/10.1016/j.euromechsol.2012.02.009>
- Shillings C, Javier C, Leblanc J, Tilton C, Corvese L, Shukla A (2017) Experimental and computational investigation of the blast response of carbon-epoxy weathered composite materials. *Compos B Eng* 129:107–116. <https://doi.org/10.1016/j.compositesb.2017.07.023>
- Shirrell C, Halpin J (1977) Moisture absorption and desorption in epoxy composite laminates. In: *Composite materials: testing and design* (fourth conference). <https://doi.org/10.1520/stp26963s>

- Tual N, Carrere N, Davies P, Bonnemains T, Lolive E (2015) Characterization of sea water aging effects on mechanical properties of carbon/epoxy composites for tidal turbine blades. *Compos A Appl Sci Manuf* 78:380–389. <https://doi.org/10.1016/j.compositesa.2015.08.035>
- Vaughan R, Gilbert J (2001) Analysis of graphite reinforced cementitious composites. NASA Report. Document ID 20010069262. <https://ntrs.nasa.gov/archive/nasa/casi.ntrs.nasa.gov/20010069262.pdf>. Accessed 10 Oct 2017
- Wei X, Espinosa HD (2013) Experimental and theoretical studies of fiber-reinforced composite panels subjected to underwater blast loading. *Blast Mitig* 91–122. https://doi.org/10.1007/978-1-4614-7267-4_4